

Multicoil Dixon Chemical Species Separation With an Iterative Least-Squares Estimation Method

Scott B. Reeder,* Zhifei Wen, Huanzhou Yu, Angel R. Pineda, Garry E. Gold, Michael Markl, and Norbert J. Pelc

This work describes a new approach to multipoint Dixon fat–water separation that is amenable to pulse sequences that require short echo time (TE) increments, such as steady-state free precession (SSFP) and fast spin-echo (FSE) imaging. Using an iterative linear least-squares method that decomposes water and fat images from source images acquired at short TE increments, images with a high signal-to-noise ratio (SNR) and uniform separation of water and fat are obtained. This algorithm extends to multicoil reconstruction with minimal additional complexity. Examples of single- and multicoil fat–water decompositions are shown from source images acquired at both 1.5T and 3.0T. Examples in the knee, ankle, pelvis, abdomen, and heart are shown, using FSE, SSFP, and spoiled gradient-echo (SPGR) pulse sequences. The algorithm was applied to systems with multiple chemical species, and an example of water–fat–silicone separation is shown. An analysis of the noise performance of this method is described, and methods to improve noise performance through multicoil acquisition and field map smoothing are discussed. Magn Reson Med 51:35–45, 2004. © 2003 Wiley-Liss, Inc.

Key words: fat suppression; musculoskeletal imaging; cardiac imaging; magnetic resonance imaging; steady-state free precession; fast spin echo; phased-array coils; silicone

Steady-state free precession (SSFP) is a rapid, short-TR imaging technique that offers specific advantages over short-TR gradient-echo techniques, including a high signal-to-noise ratio (SNR) and favorable contrast behavior. This is especially true for the visualization of fluid, because its contrast depends upon both T_1 and T_2 (1–3). However, the use of SSFP has been limited by the fact that fluid and fat both appear bright on SSFP images. This characteristic of SSFP may cause abnormalities to appear similar to normal fat and thus obscure underlying pathology.

The application of a Dixon fat–water separation method to SSFP imaging could potentially provide homogeneous and reliable separation of fat and water from SSFP images (4,5). Current methods for SSFP fat suppression include fluctuating equilibrium magnetic resonance (FEMR), linear combination SSFP, and fat-suppressed SSFP. However, all of these techniques are sensitive to field heterogeneities (6–8). The notion of combining Dixon methods with SSFP is challenging for several reasons. First, SSFP requires short repetition times (TRs) to prevent image deg-

radation from field heterogeneities (1,2). This constraint limits TE increments to values that are smaller than those traditionally used in three-point Dixon methods (5). In addition, resonant frequency offsets from chemical shift and field heterogeneities produce additional phase shifts that are unique to SSFP and are problematic for Dixon fat–water decomposition techniques (2,6).

The application of Dixon imaging in fast spin-echo (FSE) sequences has also been limited because the acquisition of echoes at different time shifts with respect to the SE increases the spacing between successive refocusing pulses (echo spacing) (9). Increasing the echo spacing reduces the number of echoes that can be collected in a time that maintains acceptable blurring from T_2 decay (10), offsetting the scan time benefits of FSE. A fat–water separation method that would permit shorter time increments would reduce the time between refocusing pulses and be beneficial to FSE imaging.

Dixon fat–water decomposition techniques have historically been limited to single-coil acquisitions because decomposition algorithms require phase unwrapping algorithms that are problematic when multiple surface coils are involved. Fat–water decomposition with multicoil reception in combination with phase unwrapping algorithms was recently reported (11).

In this work, we describe a new method for implementing Dixon fat–water separation utilizing an iterative least-squares method that reconstructs data acquired at short echo time (TE) increments, yielding images with high SNR and uniform separation of fat signal from water signal. This algorithm extends naturally to multicoil reconstruction with minimal additional complexity. Single- and multicoil decompositions derived from images obtained at both 1.5T and 3.0T are shown. In addition, examples of fat–water separation in the knee, ankle, pelvis, and heart are shown with SSFP, FSE, and other pulse sequences. The algorithm is also applied to separation of multiple chemical species, and examples of water–fat–silicone separation are provided. The noise performance of this method is analyzed, and methods to improve noise performance through field map smoothing are discussed.

THEORY

The application of traditional three-point Dixon fat–water separation to SSFP and FSE has been challenging. The three-point methods described previously by Glover (5) involved the special case of phase shifts of 0, π , and 2π , which correspond to TE increments of 0, 2.2, and 4.4 ms at 1.5T; and 0, 1.1, and 2.2 ms at 3T. Unfortunately, such TE increments cause significant lengthening of the minimum TR for SSFP, and the minimum time between refocusing

Department of Radiology, Stanford University Medical Center, Stanford, California

*Correspondence to: Scott B. Reeder, M.D., Ph.D., Rm. H1306, Department of Radiology, Stanford University Medical Center, 300 Pasteur Ave., Stanford, CA 94304. E-mail: sreeder@stanford.edu

Received 8 July 2003; revised 2 August 2003; accepted 2 August 2003.

DOI 10.1002/mrm.10675

Published online in Wiley InterScience (www.interscience.wiley.com).

© 2003 Wiley-Liss, Inc.

pulses for FSE. When SSFP is used, increases in TR can lead to severe image degradation from banding artifacts caused by off-resonance field heterogeneities and chemical shift. When applied to FSE, this method increases echo spacing by 4.4 ms at 1.5T, limiting the maximum echo train length in order to prevent blurring from T_2 decay, as well as the number of slices per unit scan time. A recently described modified three-point method that acquires images at phase shifts of 0, $\pi/2$, and π , acquiring images at 0, 1.1, and 2.2 ms at 1.5T has been applied to FSE and partially alleviates this problem. This method is restricted to a specific TE increment (12).

In this current study, an iterative linear least-squares approach was formulated, and a generalized algorithm with arbitrary TEs and multiple chemical species was developed, as described below. We discuss its extension to multicoil applications, and present an algorithm that summarizes our approach to decomposition of each chemical species. Finally, a noise analysis of this algorithm is provided.

Signal Model

Consider the signal in an image from a pixel containing M species, each with chemical shift (Hz), Δf_j ($j = 1, \dots, M$) located at position \mathbf{r} , acquired at a TE, t ,

$$s(t) = \left(\sum_{j=1}^M \rho_j e^{i2\pi\Delta f_j t} \right) e^{i2\pi\psi t} \quad [1]$$

where ρ_j is the intensity of the j th species and is, in general, a complex term with its own magnitude, $|\rho_j|$, and phase, ϕ_j , and ψ is the local magnetic resonance offset (Hz). If measurements are made at discrete echo times, t_n ($n = 1, \dots, N$), then,

$$s_n = \left(\sum_{j=1}^M \rho_j e^{i2\pi\Delta f_j t_n} \right) e^{i2\pi\psi t_n} \quad [2]$$

representing the signal in a pixel located at position \mathbf{r} , at echo time, t_n . For FSE, t_n is the shift from the center of the spin echo that occurs at $t_n = 0$. Equation [2] contains M complex unknowns (ρ_j , $j = 1, \dots, M$) and one scalar unknown (ψ), for a total of $2M + 1$ unknowns. Each image contributes a real and imaginary measurement, constituting two measurements per time point, t_n . Therefore, in general, $M + 1$ or more images are required to determine the system and separate all chemical species. For example, in a system with fat and water, $M = 2$, and at least three or more images are required to separate fat and water.

Least-Squares Estimation of Fat and Water Images

If an initial estimate of the field map, ψ_o is known, then Eq. [2] can be rewritten as

$$\hat{s}_n = s_n e^{-i2\pi\psi_o t_n} = \sum_{j=1}^M \rho_j e^{i2\pi\Delta f_j t_n}. \quad [3]$$

Equation [3] is a linear system of complex equations that can be split into real (\hat{s}_n^R) and imaginary (\hat{s}_n^I) parts,

$$\hat{s}_n = \hat{s}_n^R + i\hat{s}_n^I = \sum_{j=1}^M (\rho_j^R c_{jn} - \rho_j^I d_{jn}) + i \sum_{j=1}^M (\rho_j^R d_{jn} + \rho_j^I c_{jn}) \quad [4]$$

where ρ_j^R and ρ_j^I are the real and imaginary components of the j th species, $c_{jn} = \cos(2\pi\Delta f_j t_n)$ and $d_{jn} = \sin(2\pi\Delta f_j t_n)$. Equation [4] forms a set of linear equations that are amenable to linear least-squares fitting to decompose estimates of each chemical species. A detailed description is provided in Appendix A.

The initial estimate of the field map (ψ_o) is then refined further by defining error terms: $\psi = \psi_o + \Delta\psi$, $\rho_j^R = \hat{\rho}_j^R + \Delta\rho_j^R$, and $\rho_j^I = \hat{\rho}_j^I + \Delta\rho_j^I$ ($j = 1, \dots, M$). Inserting these expressions into Eq. [2], estimates of $\Delta\psi$, $\Delta\rho_j^R$ and $\Delta\rho_j^I$ can be calculated in the least-squares sense. Details are described in Appendix B. Mathematics particular to the special case for systems that contain only water and fat are described in Appendix C.

Algorithm for Single-Coil Acquisitions

Using the above equations and those in the appendices, the following algorithm summarizes the method used to determine the least-squares estimates of water images and fat images for each pixel:

1. Estimate the signal from each chemical species using Eq. [A3] and an initial guess for the field map, ψ_o . A useful initial guess for ψ_o is zero (Hz).
2. Calculate the error to the field map, $\Delta\psi$, using Eq. [B7].
3. Recalculate $\psi = \psi_o + \Delta\psi$.
4. Recalculate \hat{s}_n (Eqs. [3] and [4]) with the new estimate of ψ .
5. Repeat the preceding three steps until $\Delta\psi$ is small (e.g., < 1 Hz).
6. Spatially filter (smooth) the final field map, ψ , with a low-pass filter.
7. Recalculate the final estimate of each chemical species image with Eq. [A3].

The final field map is filtered to improve noise performance, as discussed below.

Multicoil Acquisition and Reconstruction Algorithm

A multicoil acquisition with P elements collects P independent images, all with a different relative phase offsets. By using the algorithm described above, P images of each chemical species are generated, as well as P field heterogeneity maps, which should not depend on coil-dependent phase shifts. The field maps are then combined by weighting the contribution from each coil by the square of the magnitude of the image contributed by that coil, in a manner similar to that used in standard multicoil image combinations (13–15). Specifically, for each pixel the combined field map is calculated as

$$\psi_c = \frac{\sum_{p=1}^P \psi_p |s_p|^2}{\sum_{p=1}^P |s_p|^2}. \quad [5]$$

Using the combined field map, \hat{s}_n is recalculated with Eq. [4], and new estimates of the P images of the different chemical species are calculated from Eq. [A3]. Finally, the P images for each chemical species are combined using a common multicoil reconstruction as previously described (13–15).

A summary of the final chemical species decomposition is provided below, which accounts for multicoil acquisitions, and smoothing of the final field map:

1. For each coil and each pixel.
 - a. Estimate each chemical species assuming an initial guess for the field map, ψ_o , from Eq. [A3].
 - b. Calculate the error to the field map, $\Delta\psi$, from Eq. [B7].
 - c. Recalculate $\psi = \psi_o + \Delta\psi$.
 - d. Recalculate \hat{s}_n (Eqs. [3] and [4]) with the new estimate of ψ .
 - e. Repeat the process until $\Delta\psi$ is small.
2. If this is a multicoil acquisition, combine P field maps into a combined field map using Eq. [5].
3. Spatially filter (smooth) the field map with a low-pass filter.
4. Recalculate the final images for each chemical species with Eq. [A3] for each coil.
5. For multicoil acquisitions, combine the final images for each chemical species from each coil using standard multicoil combination techniques.

Noise Considerations

In the presence of noise with variance σ^2 , the covariance matrix of the estimate of $\hat{\rho}$ from Eq. [A3] is (16)

$$\text{cov}(\hat{\rho}) = \sigma^2 (\mathbf{A}^T \mathbf{A})^{-1} \quad [6]$$

if it assumed that the field heterogeneity map, ψ , is known. The diagonal elements of $\text{cov}(\hat{\rho})$ represents the Cramer-Rao bound, or lowest possible limit of the error variance of the M th species. In the specific case of water and fat, with equal TE spacing of increment Δt , such that $t_n = t_o + n\Delta t$, with $n = 0, 1, \dots, N-1$, the fat and water estimates have equal variance and are determined from the diagonal terms of the covariance matrix calculated from Eq. [6]

$$\text{var}(\hat{\rho}) = \frac{N\sigma^2}{N^2 - \frac{\sin^2 N\theta}{\sin^2 \theta}} \quad [7]$$

where $\theta = \pi \Delta f_{fw} \Delta t$, and it has been assumed that the real and imaginary parts of the signal are uncorrelated and have equal variance. As described by Glover (5), the effective number of signal averages (NSA) is

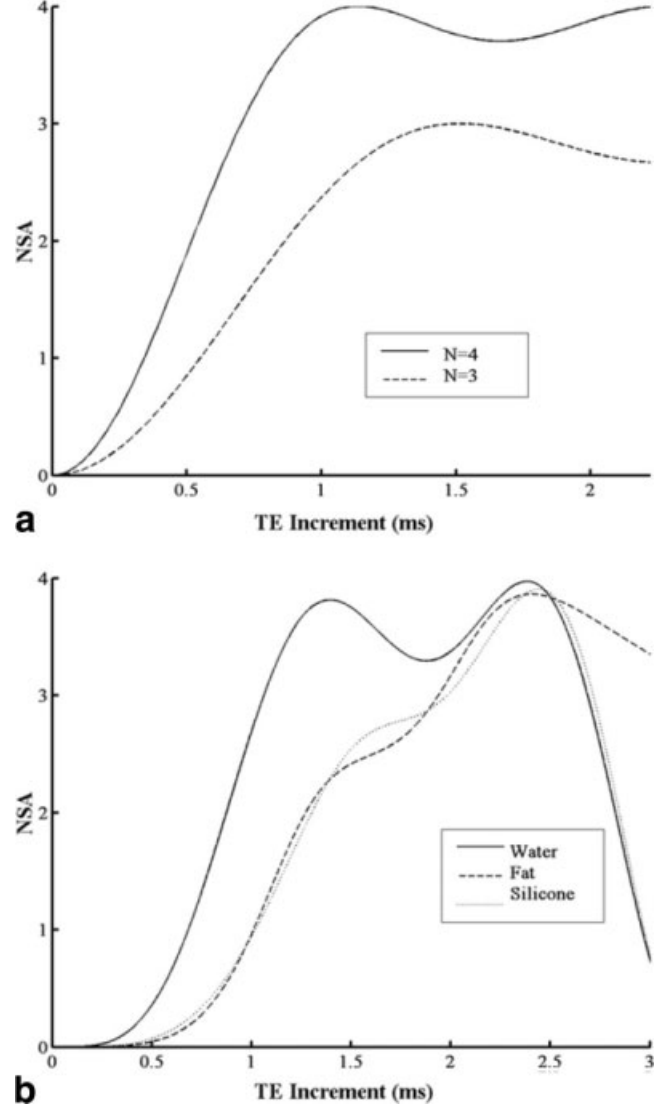


FIG. 1. **a:** Dependence of the effective NSA on the TE increment (ms) from fat–water chemical shift for three-echo (solid) and four-echo (dashed) acquisitions at 1.5T. **b:** NSA for water, fat, and silicone for a four-echo acquisition to resolve all three species at 1.5T.

$$NSA = \frac{\sigma^2}{\text{var}(\hat{\rho})}. \quad [8]$$

This is a helpful way to describe the effect of Δt on the noise behavior of a multipoint fat–water separation. Therefore, for evenly spaced TEs, the effective NSA is

$$NSA = N - \frac{1}{N} \frac{\sin^2 N\theta}{\sin^2 \theta}. \quad [9]$$

This represents the upper limit of effective signal averaging and noise performance for any N -point fat–water estimation technique. The optimal TE spacing that maximizes NSA occurs when $N\theta = \pi$, such that $\Delta t = 1/N\Delta f_{fw}$, which is an intuitive result reflecting the fact that optimal sampling should occur when the phase differences between fat

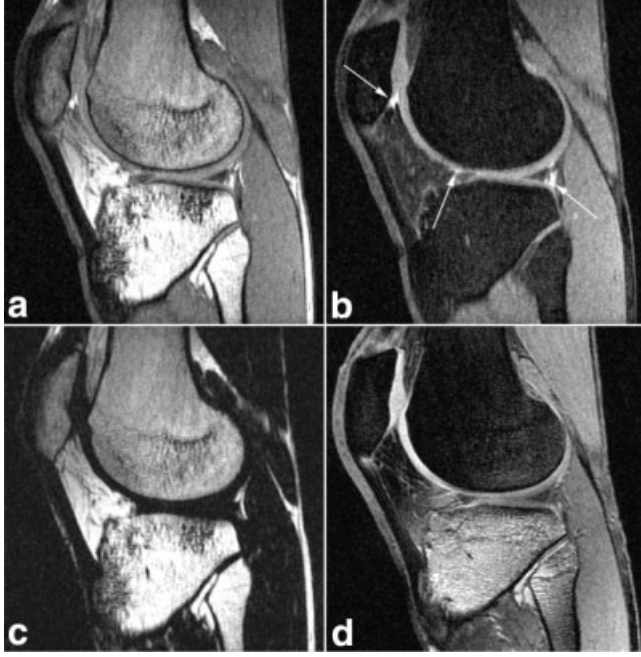


FIG. 2. Sagittal SSFP images obtained in the knee of a human volunteer at 1.5T. Source (a), calculated water (b), calculated fat (c) images are shown in comparison with an FS-SPGR image (d). Excellent fat–water suppression was obtained with the SSFP images, and the joint fluid appears bright (arrows). This creates an arthrographic effect that improves the conspicuity of cartilage defects. Four source images (TE = 1.2, 2.1, 3.0, 3.9 ms) were acquired. TR = 6.1 ms, image matrix = $256 \times 192 \times 64$, and bandwidth = ± 125 kHz.

and water are evenly distributed around the unit circle. At this echo spacing, NSA = N , demonstrating that for images acquired at the optimal echo spacing, the SNR of the calculated water and fat images is equivalent to the average of N source images. Therefore, multipoint Dixon decomposition performed at the optimal TE spacing is efficient in terms of SNR.

Figure 1a plots Eq. [9] for $N = 3$ and $N = 4$ at 1.5T, representing the upper limits of noise performance for a multipoint fat–water decomposition, assuming that the relative chemical shift of fat and water is -3.5 ppm ($\Delta f_{fw} = -220$ Hz at 1.5T). For example, the optimal echo spacing at 1.5T is 1.5 ms for three equally spaced echoes, and 1.1 ms for a four-echo acquisition.

In the case of three species, the calculated values of NSA are not equal for each of the three species. For such a system, the NSA for each of the three species is:

$$NSA_w = N + \frac{(2ABC - N(A^2 + B^2))}{N^2 - C^2} \quad [10a]$$

$$NSA_f = N + \frac{(2ABC - N(A^2 + C^2))}{N^2 - B^2} \quad [10b]$$

$$NSA_s = N + \frac{(2ABC - N(B^2 + C^2))}{N^2 - A^2} \quad [10c]$$

where $A = \frac{\sin(\pi\Delta f_{12}N\Delta t)}{\sin(\pi\Delta f_{12}\Delta t)}$, $B = \frac{\sin(\pi\Delta f_{13}N\Delta t)}{\sin(\pi\Delta f_{13}\Delta t)}$, $C = \frac{\sin(\pi\Delta f_{23}N\Delta t)}{\sin(\pi\Delta f_{23}\Delta t)}$, and Δf_{12} , Δf_{13} , and Δf_{23} are relative chemical shifts of species 1–2, species 1–3, and species 2–3, respectively. Figure 1b plots Eqs. [10a]–[10c] assuming the chemical shifts of fat and silicone relative to water are -3.5 ppm (-220 Hz at 1.5T) and -4.9 ppm (-310 Hz at 1.5T), respectively (17). From this figure, the increment in TE that optimizes the noise performance for silicone, fat, and water is approximately 2.4 ms at 1.5T.

MATERIALS AND METHODS

Images of human volunteers were obtained on 1.5T GE CV/i, 1.5T GE TwinSpeed, and 3.0T GE VH/i scanners. A standard extremity coil was used to image the knee and ankle at 1.5T, a prototype phased-array multicore was used for the knee and ankle at 3.0T, and a standard phased-array torso coil was used to image the heart, pelvis, and abdomen at 1.5T. The study was approved by our institutional review board. Prior to imaging, informed consent was obtained from the volunteers. Product automated shim routines were used for all imaging.

3D-SSFP imaging was performed in the knee, ankle, and pelvis. The typical imaging parameters for the knee and ankle included $N_x = 256$ (fractional readout), $N_y = 192$, NSA = 1, FOV = 16 cm, slice = 1.5 mm, $N_z = 32$ –64, TR = 5.6–6.2, and three or four echoes spaced by approximately 1 ms (1.5T) and 0.5 ms (3.0T). Bandwidth at 1.5T was ± 125 kHz and ± 42 kHz at 3.0T. The imaging parameters in the pelvis included $N_x = 512$, $N_y = 256$, NSA = 1, FOV = 32 cm, slice = 4 mm, $N_z = 32$, TR = 5.5 ms, and three echoes (TE = 0.9, 1.9, 2.9 ms).

To demonstrate the ability of the Dixon method to separate fat and water in the presence of a heterogeneous magnetic field, 3D spoiled gradient-echo (SPGR) images with fat saturation were obtained in the knee and ankle at both 1.5T and 3.0T. The matrix size, field of view (FOV), and slice thickness were the same as in the SSFP images. Other parameters included TR = 50 ms, TE = 5 ms (full echo), tip angle = 40° , and BW = ± 16 kHz. These parameters were based on established protocols using fat-saturated SPGR (FS-SPGR) imaging for articular cartilage (18,19). The total scan time for a 64-slice FS-SPGR set of images was 12:04 min. Comparison fat-saturated FSE images were also obtained in the abdomen, with the same imaging parameters used for the Dixon acquisition, except that three signal averages were used to obtain comparable SNR.

Cardiac images were acquired at 1.5T with a modified 2D retrospectively gated SSFP sequence, with the following imaging parameters: $N_x = 224$ (fractional readout), $N_y = 128$, NSA = 1, FOV = 32 cm, slice = 8 mm, TR = 5.2, and three echoes (TE = 0.9, 1.9, 2.9). Twenty phases were acquired through systole and diastole with a segmentation factor of 16 for a time resolution of 83 ms. The total breath-hold time for one slice was approximately 20–24 s, depending on the heart rate.

FSE images were acquired in the knee and abdomen. In the knee, the imaging parameters included BW = ± 16 kHz, $N_x = 320$, $N_y = 224$, NSA = 1, FOV = 16 cm, slice =



FIG. 3. Sagittal SSFP images obtained in the ankle of a human volunteer at 3.0T. Source (a), calculated water (b), and calculated fat (c) images are shown in comparison with an FS-SPGR image (d). Compared to the FS-SPGR image, excellent fat–water suppression was obtained with the SSFP images, and the joint fluid appears bright. Three source images were acquired ($TE = 1.4, 1.9, 2.4$ ms), $TR = 5.6$, image matrix = $256 \times 192 \times 32$, and bandwidth = ± 42 kHz.

2 mm, $TR = 5000$ ms, effective $TE = 10$ ms, echo spacing = 13.6 ms, and three TE increments ($\Delta TE = -1.0, 0, 1.0$ ms). In the abdomen, the imaging parameters included a torso phased-array coil, respiratory triggering, $BW = \pm 31.3$ kHz, $N_x = 384$, $N_y = 192$, $NSA = 1$, $FOV_x = 34$ cm, $FOV_y = 25.5$ cm, slice = 8 mm, effective $TE = 90$ ms, echo spacing = 13.6 ms, and three TE increments ($\Delta TE = -1$ ms, 0 ms, 1 ms). For comparison, fat-saturated FSE images were obtained with identical imaging parameters and $NSA = 3$.

SPGR imaging of a silicone-fat-water phantom was performed at 1.5T using a standard head coil. Parts A and B of a Sylgard 527 dielectric silicone gel (Dow Corning, Midland, MI) were mixed at a ratio of 6:7 and allowed to set in 15-cc and 50-cc vials. Olive oil was placed in 15-cc and 50-cc vials, and all vials were placed in a 1-liter vessel containing tap water. Imaging parameters included $BW = \pm 31.3$ kHz, $N_x = 256$, $N_y = 256$, $NSA = 4$, $FOV = 16$ cm, slice = 4 mm, $TR = 34$ ms, and $TE = 4.9, 7.3, 9.7, 12.1$ ms.

An offline reconstruction program written in Matlab 6.0 (The Mathworks, Natick, MA) was used to perform fast Fourier transform reconstruction of all images. After the complex (magnitude and phase) images were reconstructed, the water and fat images were estimated according to the iterative least-squares algorithm described above. The field maps were smoothed with a 3×3 boxcar filter.

RESULTS

Examples of the source SSFP and FSE images, and the calculated water and fat images are shown in Figs. 2–7 and

8–10. Uniform fat–water separation was achieved in all images, with relatively short acquisition times. In SSFP imaging, fluid appears bright. This is particularly helpful in musculoskeletal imaging because it provides an arthrographic effect that increases the conspicuity of cartilage defects. For example, a small focal cartilage defect in the anterior tibial cartilage of the ankle is easily seen in the water image in Fig. 5.

The cardiac SSFP images demonstrated uniform fat–water separation with good spatial and temporal resolution, acquired within one breath-hold (Fig. 7). Flow artifact was minimal, and excellent fat–water separation was achieved.

Uniform fat separation was seen with multicoil SSFP and FSE imaging in the pelvis and abdomen (Figs. 6 and 10). A rim of high signal is seen anteriorly within the FSE-calculated water image (Fig. 10b). This was caused by a small misregistration between sequential source images that were acquired during free breathing with respiratory triggering.

Excellent separation of silicone, fat, and water was also achieved in a phantom using SPGR imaging (Fig. 11). Four source images with TE increments of 2.4 ms were used to optimize the SNR of this decomposition, as described in Eqs. [10a]–[10c] and visualized explicitly in Fig. 1b.

DISCUSSION

In this work we have demonstrated the feasibility of using a multipoint Dixon chemical shift separation technique that employs multiple images acquired at arbitrary TE increments to separate each species with a unique chemical shift. An iterative least-squares fitting algorithm was described and implemented with pulse sequences (such as SSFP and FSE) that benefit from short TE increments to maintain good image quality. This algorithm allows for optimization of SNR performance, as well as tradeoffs between acquisition parameters and SNR. In addition, phase-unwrapping algorithms are not necessary with this approach. (Such algorithms are commonly used with Dixon fat–water separation techniques, and add tremendously to the complexity of the reconstruction algorithm.) The approach was also extended to multicoil acquisitions, with minimal increase in complexity. In vivo examples from the knee, ankle, pelvis, and heart were shown, demonstrating excellent fat–water separation. In all cases, uniform separation of all chemical species was achieved with excellent image quality and high SNR. One advantage of Dixon techniques over fat-suppression techniques is that the source images (as well as fat images) are available and can contribute to the diagnostic value of the study.

Artifacts will result if source images are not registered with one another, as shown in Fig. 10. Registration of source images in musculoskeletal imaging was not problematic, and registration in cardiac imaging was achieved by acquiring all images within one breath-hold. In the presence of arrhythmias, misregistration of cardiac source images could potentially occur. Imaging in the pelvis was also not problematic; however, imaging in the abdomen was more difficult because of misregistration from respiratory motion. Possible solutions for these problems include reducing scan times so that images can be acquired

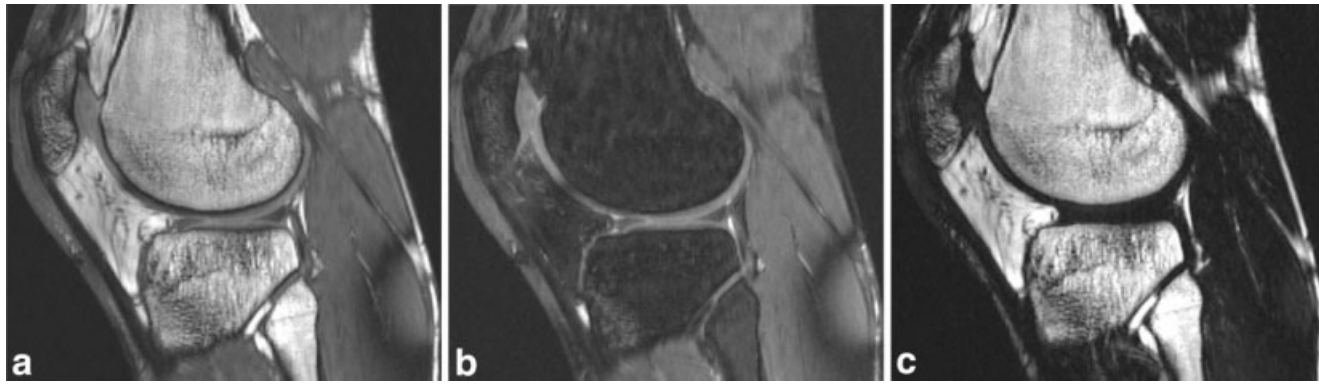


FIG. 4. Sagittal SSFP images from the knee of a human volunteer at 3.0T with (a) source, (b) calculated water, and (c) calculated fat images. Uniform fat–water separation is identified and the joint fluid appears bright. Three source images were acquired ($TE = 1.4, 1.9, 2.4$ ms). $TR = 5.6$ ms, image matrix = $256 \times 192 \times 32$, and bandwidth = ± 42 kHz.

within one breath-hold, and using interleaving echoes for different source images so that the data can be registered more closely.

The mathematics of this technique were generalized to include systems with multiple chemical species, such as silicone, fat, and water. The simultaneous separation of these three species may be helpful in assessments of breast-implant integrity. In this study, silicone–fat–water separation was demonstrated in a phantom. In a previous study employing traditional three-point Dixon imaging (17), the fortuitous relative chemical shifts of silicone, water, and fat were exploited to effect the separation of water and fat into one image and silicone into a second image.

In the noise analysis presented above, it was assumed that the field map was known precisely. However, in general this is not the case, and the estimate of the field map itself is calculated from source images, which contain noise. This in turn will degrade the noise performance of the final estimates of water and fat images, and a complete description of the noise performance of multipoint fat–water decomposition must reflect the fact that the field

map is an unknown quantity. The effect of estimating the field map degrades the noise performance of the water and fat estimation from that described in Eq. [9].

Other factors in a noise analysis must also be considered. For example, if it is assumed that the field map is smoothly varying in space, then spatial smoothing of the final estimate of the field map will improve the SNR performance of the estimation algorithm. An alternative to smoothing the calculated field map is to smooth the source images (20,21). In addition, the combination of separate field maps calculated in a multicoil algorithm further improves SNR performance of field map estimation by combining multiple contributions to the local field map. However, the description above (summarized in the special case described in Eq. [9]) is very useful because it acts as an upper limit for the best achievable SNR performance for the estimation of water and fat, and describes the effects of the TE increment. Improvements in the noise performance of the field map estimation through smoothing and multicoil acquisitions will improve the NSA for water and fat, but cannot exceed this upper limit. A detailed mathematical description that includes the effects of field map esti-



FIG. 5. Sagittal SSFP images of an ankle at 1.5T with (a) source, (b) calculated water, and (c) calculated fat images. Uniform fat–water separation is identified and the joint fluid appears bright. A small defect in the anterior tibial cartilage (arrow) is well delineated by the joint fluid, which appears bright. Four source images were acquired ($TE = 1.2, 2.1, 3.0, 3.9$ ms). $TR = 6.1$ ms, image matrix = $256 \times 192 \times 64$, and bandwidth = ± 125 kHz.

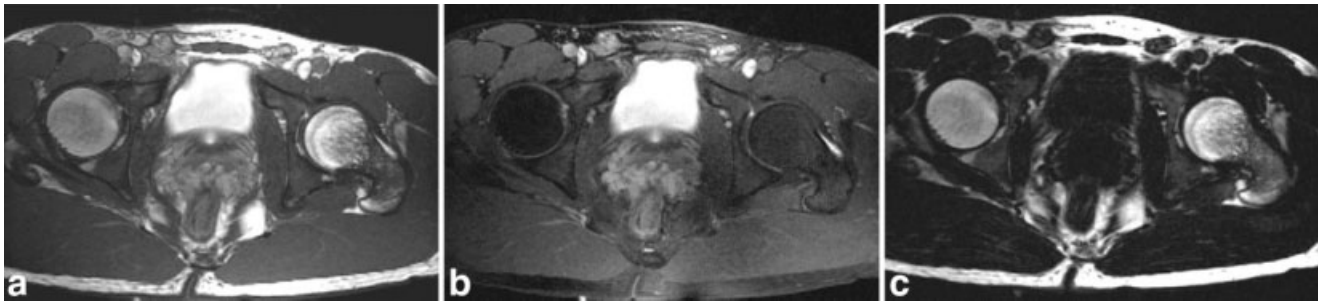


FIG. 6. Axial SSFP images obtained in the pelvis of a human volunteer at 1.5T. Source (a), calculated water (b), and calculated fat (c) images demonstrate uniform fat–water separation and good image quality. Three source images were acquired ($TE = 0.8, 1.8, 2.8$ ms). $TR = 5.4$ ms, image matrix = $512 \times 256 \times 32$, and bandwidth = ± 125 kHz.

mation, smoothing of field maps or source images, and multicoil acquisitions is complex and beyond the scope of this work.

The extension of the least-squares iterative algorithm to multicoil acquisitions was straightforward. The calculated field map for each coil is independent of local phase shifts that may differ between coils, which allows the field maps to be easily combined through well-described multicoil combination methods. This obviated the need for complex phase unwrapping algorithms applied to the multicoil source data. Combining field maps using multicoil acquisitions also improves the local SNR of the field map, and thus improves the noise performance of the water and fat estimation.

The shorter TE increments used in this work helped alleviate the large increases in TR with SSFP, and echo spacing with FSE, that are necessary with standard (5) and modified (12) three-point Dixon techniques. In general, any technique that shifts echo times will increase TR and echo spacing. Therefore, this approach is limited in circumstances where the TR (SSFP) and echo spacing (FSE) must be kept very short. Recent work by Ma et al. describes a three-point “Dixon” method that acquires FSE source images at different effective echo times through the use of shifted fractional echoes (22) and a reconstruction algorithm akin to homodyne reconstruction (23). This allows data to be acquired with echoes that are sufficiently spaced to separate fat and water, with minimal increases in the echo spacing. The same approach should be effective with

the technique described above. However, in the current study the increase in echo spacing was relatively minimal with the low bandwidths that were used, and the approach described in Ref. 22 would be most beneficial in FSE applications that use high bandwidths. The application of that approach to SSFP imaging would also help maintain short TRs and thus prevent image degradation from banding caused by field heterogeneities.

Although fat–water separation with the method described in this work is efficient from an SNR perspective, the acquisition of a minimum of three echoes can be limiting—especially in cardiac imaging, where all data must be acquired within one breath-hold. Various strategies can be employed to reduce the total acquisition time. Many of these approaches assume that the field heterogeneity map varies smoothly across the object, and sampling the central portions of k -space may be adequate to estimate the field map. A simple way to reduce scan time would be to acquire some source images with a reduced matrix size. For example, in a three-echo acquisition scheme, a reduction in the number of k_y (phase-encoding) lines of one source image would permit the calculation of a low-resolution field heterogeneity map, while reducing total scan time. With this low-resolution field map and two full-resolution source images, estimates of water and fat images could then be made.

Additional time savings could be made with pulse sequences that acquire multiple images in a time sequence,

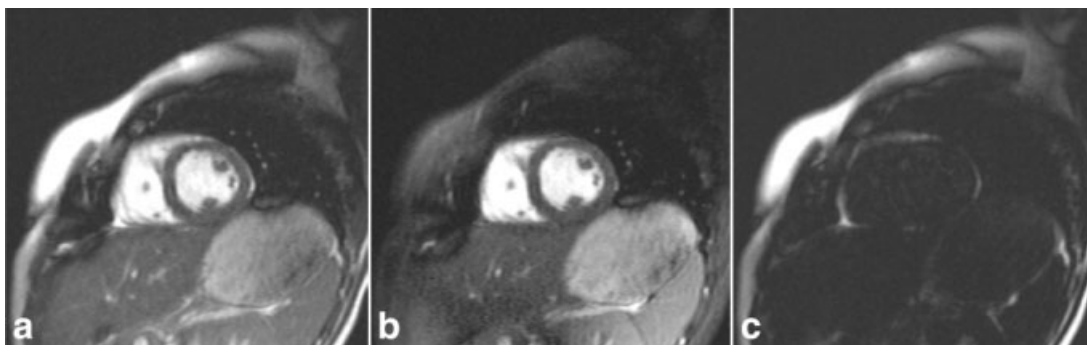


FIG. 7. Short-axis CINE SSFP cardiac images acquired with a torso phased-array coil. The source image (a), calculated water image (b), and calculated fat image (c) are shown at one phase (of 20 phases). Uniform fat–water separation was consistently achieved in all slices and phases. Three source images were acquired ($TE = 0.9, 1.9, 2.9$ ms). $TR = 5.2$ ms, image matrix = 224×128 , and bandwidth = ± 125 kHz.



FIG. 8. Sagittal proton density FSE images from the knee of a human volunteer acquired at 1.5T with (a) source, (b) calculated water, and (c) calculated fat images. Uniform fat–water separation was achieved and the joint fluid appears bright. Three source images were acquired (shift in TE = −1.0, 0, 1.0 ms). TR = 5000 ms, effective TE = 10 ms, image matrix = 320×224 , echo spacing = 13.7 ms, and bandwidth = ± 20.8 kHz.

such as cardiac CINE imaging, in which the field maps can be assumed to vary little in time (24). Field maps that are calculated for one image could be used for fat–water separation in multiple images, reducing the amount of required data dramatically.

The acquisition of multiple echoes within one TR, such as in a multiecho SSFP (25) or gradient-echo SE (GRASE) (26) sequence, could also exploit the evolving phase of spins with different chemical shifts. The mathematics of such reconstruction schemes are more complex and must consider additional phase shifts and differential time delays between echoes acquired with different gradient polarities (27).

In systems where low bandwidths are used and significant chemical shift artifacts are present in the readout direction, Dixon imaging could potentially be used to correct for such artifacts. This could be accomplished by decomposing the chemical species as described in this work, and then shifting each calculated image by an

amount depending on its chemical shift and the acquisition bandwidth. Distortion from susceptibility could also be corrected because the field map would be known. Finally, the corrected images would be recombined into a corrected image free from chemical shift and distortion in the readout direction. A similar approach using subsequent acquisition of selective water and fat images using spectral-spatial pulses has been described (28).

CONCLUSIONS

The iterative, least-squares, multipoint fat–water separation method described in this work represents a new approach that permits the use of variable TE increments that can be exploited to optimize SNR or improve speed performance for demanding sequences such as SSFP and FSE. This approach can be used to separate systems with three distinct chemical shifts (such as silicone, fat, and water), and can also be used with multicoil imaging.

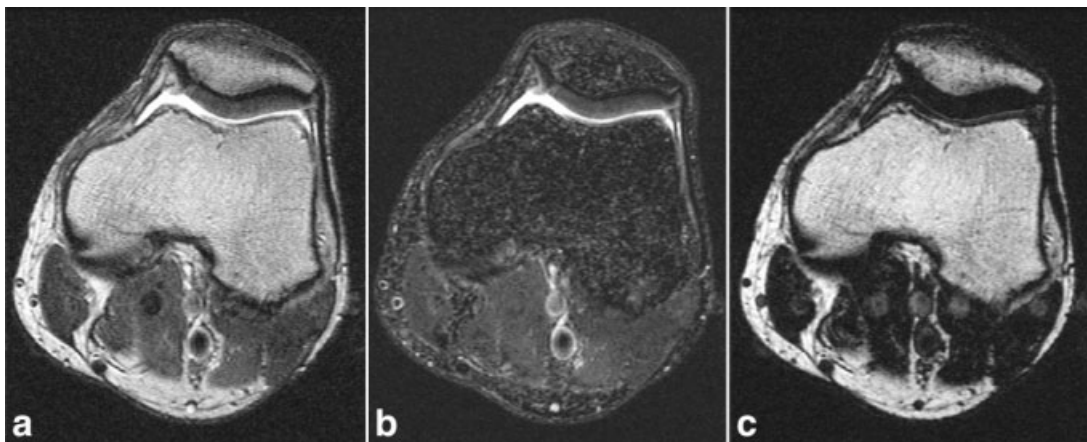


FIG. 9. Axial T_2 -weighted density FSE images from the knee of a human volunteer acquired at 1.5T with (a) source, (b) calculated water, and (c) calculated fat images. Uniform fat–water separation was achieved and the joint fluid appears bright. Three source images were acquired (shift in TE = −1.0, 0, 1.0 ms). TR = 5000 ms, effective TE = 70 ms, image matrix = 384×192 , echo spacing = 17.5 ms, and bandwidth = ± 15.6 kHz.

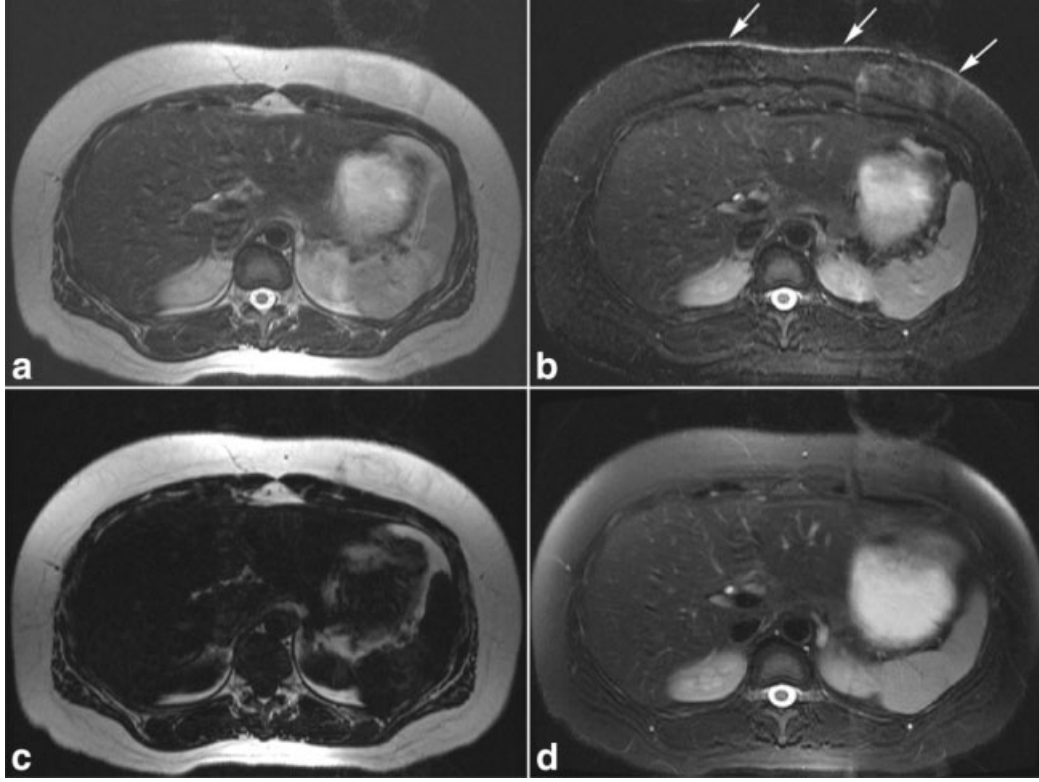


FIG. 10. Axial T_2 -weighted FSE images obtained in the abdomen of a human volunteer at the level of the spleen at 1.5 with (a) source, (b) calculated water, and (c) calculated fat images. Images were acquired with the torso phased-array coil during free breathing using respiratory triggering. Uniform fat-water separation was achieved everywhere except at the anterior skin surface, where misregistration between subsequent scans caused calculation errors (arrows). Three source images were acquired (shift in TE = -1.0, 0, 1.0 ms). Effective TE = 90 ms, image matrix = 384×192 , 3/4 FOV, echo spacing = 11.9 ms, and bandwidth = ± 31.3 kHz. d: A fat-saturated T_2 -weighted FSE image with the same imaging parameters and NSA = 3 is also shown.

ACKNOWLEDGMENTS

The authors thank Dwight Nishimura, Ph.D., Kim Butts, Ph.D., and Peter Kellman, Ph.D., for helpful discussions. We also thank Ann Shimakawa, MSE, Jean Brittain, Ph.D., and Reed Busse, Ph.D., for their assistance with the images acquired at 3.0T and FSE imaging at 1.5T.

APPENDIX A

For $n = 1, \dots, N$, Eq. [4] can be written in matrix format:

$$\hat{\mathbf{S}} = \mathbf{A}\mathbf{p} \quad [\text{A1}]$$

$$\hat{\mathbf{S}} = [\hat{s}_1^R \quad \hat{s}_1^I \quad \dots \quad \hat{s}_N^R \quad \hat{s}_N^I]^T,$$

$$\mathbf{p} = [\rho_1^R \quad \rho_1^I \quad \rho_2^R \quad \rho_2^I \quad \dots \quad \rho_M^R \quad \rho_M^I]^T,$$

$$\mathbf{A} = \begin{bmatrix} c_{11} & -d_{11} & c_{21} & -d_{21} & \dots & c_{M1} & -d_{M1} \\ c_{12} & -d_{12} & c_{22} & -d_{22} & \dots & c_{M2} & -d_{M2} \\ \dots & \dots & \dots & \dots & \dots & \dots & \dots \\ c_{1N} & -d_{1N} & c_{2N} & -d_{2N} & \dots & c_{MN} & -d_{MN} \\ d_{11} & c_{11} & d_{21} & c_{21} & \dots & d_{M1} & c_{M1} \\ d_{12} & c_{12} & d_{22} & c_{22} & \dots & d_{M2} & c_{M2} \\ \dots & \dots & \dots & \dots & \dots & \dots & \dots \\ d_{1N} & c_{1N} & d_{2N} & c_{2N} & \dots & d_{MN} & c_{MN} \end{bmatrix} \quad [\text{A2}]$$

where rows 1 to N of matrix \mathbf{A} are used to calculate the real components of the signal, and rows $N + 1$ to $2N$ are used to calculate the imaginary components of the signal. Using a well-described least-squares fitting approach for linear systems of equations (29), it can be shown that

$$\hat{\mathbf{p}} = (\mathbf{A}^T \mathbf{A})^{-1} \mathbf{A}^T \hat{\mathbf{S}} \quad [\text{A3}]$$

where $\hat{\mathbf{p}} = [\hat{\rho}_1^R \quad \hat{\rho}_1^I \quad \hat{\rho}_2^R \quad \hat{\rho}_2^I \quad \dots \quad \hat{\rho}_M^R \quad \hat{\rho}_M^I]^T$, determining initial *estimates* of each chemical species.

APPENDIX B

If $\rho_j^R = \hat{\rho}_j^R + \Delta\rho_j^R$ and $\rho_j^I = \hat{\rho}_j^I + \Delta\rho_j^I$ ($j = 1, \dots, M$), and $\psi = \psi_o + \Delta\psi$, then Eq. [2] can be written as

$$s_n \approx \left(\sum_{j=1}^M (\hat{\rho}_j + \Delta\rho_j) e^{i2\pi\Delta f_j t_n} \right) e^{i2\pi\psi_o t_n} e^{i2\pi\Delta\psi t_n}. \quad [\text{B1}]$$

Dividing each side by $e^{i2\pi\psi_o t_n}$, and using the Taylor approximation $e^{i2\pi\Delta\psi t_n} \approx 1 + i2\pi\Delta\psi t_n$, such that

$$\begin{aligned} \hat{s}_n^R + i\hat{s}_n^I &= \left(\sum_{j=1}^M (\hat{\rho}_j^R + \Delta\rho_j^R + i(\hat{\rho}_j^I + \Delta\rho_j^I))(c_{jn} + id_{jn}) \right) \\ &\quad \times (1 + i2\pi\Delta\psi t_n). \end{aligned} \quad [\text{B2}]$$

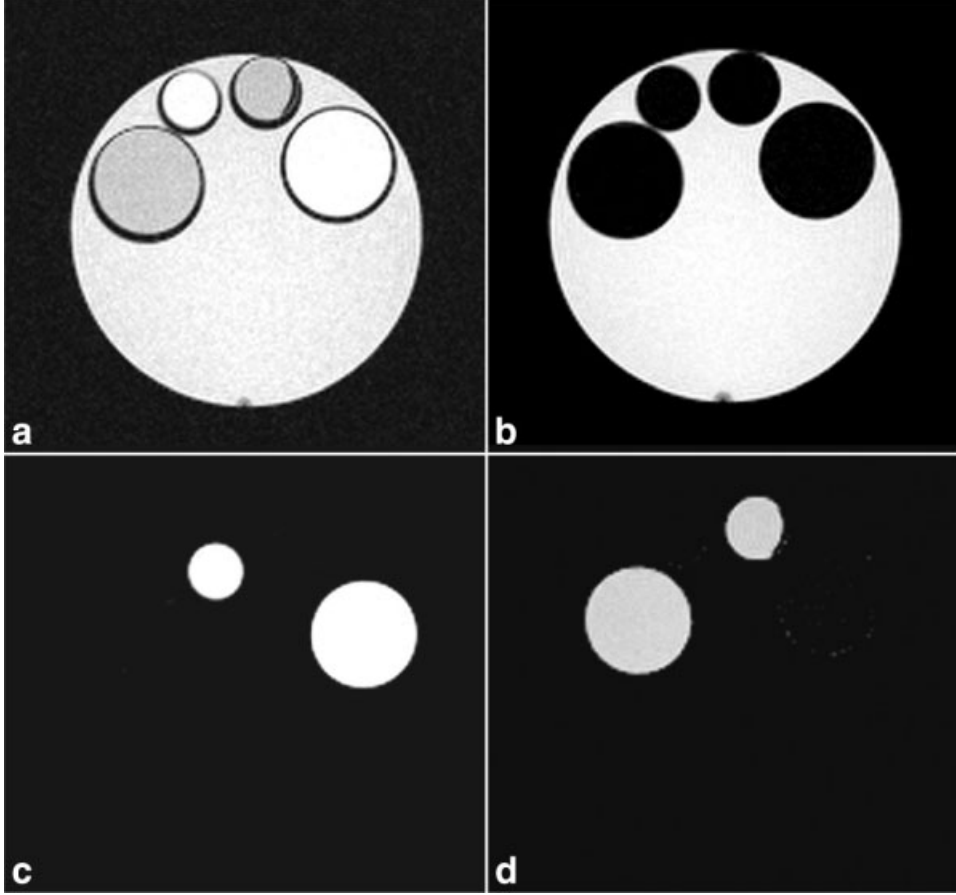


FIG. 11. SPGR (a) source, (b) calculated water, (c) calculated fat, and (d) calculated silicone images in a phantom. Four images were acquired (TE = 4.9, 7.3, 9.7, 12.1 ms). TR = 34 ms, flip angle = 10°, matrix = 256 × 256, FOV = 16 cm, bandwidth = ±31.3 kHz, and slice thickness = 4 mm.

Rearranging Eq. [B2], and splitting into real

$$\hat{s}_n^R = \hat{s}_n^R - \sum_{j=1}^M (\hat{\rho}_j^R c_{jn} - \hat{\rho}_j^I d_{jn}) = 2\pi\Delta\psi t_n \sum_{j=1}^M (-\hat{\rho}_j^R d_{jn} - \hat{\rho}_j^I c_{jn}) + \sum_{j=1}^M \Delta\rho_j^R c_{jn} - \sum_{j=1}^M \Delta\rho_j^I d_{jn} \quad [\text{B3}]$$

and imaginary components

$$\hat{s}_n^I = \hat{s}_n^I - \sum_{j=1}^M (\hat{\rho}_j^R d_{jn} + \hat{\rho}_j^I c_{jn}) = 2\pi\Delta\psi t_n \sum_{j=1}^M (\hat{\rho}_j^R c_{jn} - \hat{\rho}_j^I d_{jn}) + \sum_{j=1}^M (\Delta\rho_j^R d_{jn} + \Delta\rho_j^I c_{jn}) \quad [\text{B4}]$$

where \hat{s}_n^R and \hat{s}_n^I are defined in Eqs. [B3] and [B4]. Arranging in matrix format for $n = 1, \dots, N$:

$$\hat{\mathbf{S}} \approx \mathbf{B}\mathbf{y} \quad [\text{B5}]$$

where $\hat{\mathbf{S}} = [\hat{s}_1^R \ \hat{s}_2^R \ \dots \ \hat{s}_N^R \ \hat{s}_1^I \ \hat{s}_2^I \ \dots \ \hat{s}_N^I]^T$,

$$\mathbf{y} = [\Delta\psi \ \Delta\rho_1^R \ \Delta\rho_1^I \ \Delta\rho_2^R \ \Delta\rho_2^I \ \dots \ \Delta\rho_M^R \ \Delta\rho_M^I]^T,$$

$$g_{jn}^R = 2\pi t_n \sum_{j=1}^M (-\hat{\rho}_j^R d_{jn} - \hat{\rho}_j^I c_{jn})$$

and $g_{jn}^I = 2\pi t_n \sum_{j=1}^M (\hat{\rho}_j^R c_{jn} - \hat{\rho}_j^I d_{jn})$, such that,

$$\mathbf{B} = \begin{bmatrix} g_{11}^R & c_{11} & -d_{11} & c_{21} & -d_{21} & \dots & c_{M1} & -d_{M1} \\ g_{12}^R & c_{12} & -d_{12} & c_{22} & -d_{22} & \dots & c_{M2} & -d_{M2} \\ \dots & \dots & \dots & \dots & \dots & \dots & \dots & \dots \\ g_{1N}^R & c_{1N} & -d_{1N} & c_{2N} & -d_{2N} & \dots & c_{MN} & -d_{MN} \\ g_{11}^I & d_{11} & c_{11} & d_{21} & c_{21} & \dots & d_{M1} & c_{M1} \\ g_{12}^I & d_{12} & c_{12} & d_{22} & c_{22} & \dots & d_{M2} & c_{M2} \\ \dots & \dots & \dots & \dots & \dots & \dots & \dots & \dots \\ g_{1N}^I & d_{1N} & c_{1N} & d_{2N} & c_{2N} & \dots & d_{MN} & c_{MN} \end{bmatrix}. \quad [\text{B6}]$$

For $n = 1, \dots, N$, Eq. [B5] is also a linear system of equations, and estimates of \mathbf{y} can be calculated (29) by

$$\mathbf{y} = (\mathbf{B}^T \mathbf{B})^{-1} \mathbf{B}^T \hat{\mathbf{S}} \quad [\text{B7}]$$

which is used to determine $\Delta\psi$, $\Delta\rho_j^R$, and $\Delta\rho_j^I$.

APPENDIX C

In the special case of only water and fat (Δf_{fw} = relative fat–water chemical shift), and the receive/transmit fre-

quency of the scanner is set to the water resonance, matrices **A** and **B** become

$$\mathbf{A} = \begin{bmatrix} 1 & 0 & c_1^{fw} & -d_1^{fw} \\ 1 & 0 & c_2^{fw} & -d_2^{fw} \\ \dots & \dots & \dots & \dots \\ 1 & 0 & c_N^{fw} & -d_N^{fw} \\ 0 & 1 & d_1^{fw} & c_1^{fw} \\ 0 & 1 & d_2^{fw} & c_2^{fw} \\ \dots & \dots & \dots & \dots \\ 0 & 1 & d_N^{fw} & c_N^{fw} \end{bmatrix}$$

and

$$\mathbf{B} = \begin{bmatrix} g_1^R & 1 & 0 & c_1^{fw} & -d_1^{fw} \\ g_2^R & 1 & 0 & c_2^{fw} & -d_2^{fw} \\ \dots & \dots & \dots & \dots & \dots \\ g_N^R & 1 & 0 & c_N^{fw} & -d_N^{fw} \\ g_1^I & 0 & 1 & d_1^{fw} & c_1^{fw} \\ g_2^I & 0 & 1 & d_2^{fw} & c_2^{fw} \\ \dots & \dots & \dots & \dots & \dots \\ g_N^I & 0 & 1 & d_N^{fw} & c_N^{fw} \end{bmatrix} \quad [C1]$$

where $c_n^{fw} = \cos(2\pi\Delta f_{fw}t_n)$, $d_n^{fw} = \sin(2\pi\Delta f_{fw}t_n)$, $g_n^R = 2\pi t_n(-\hat{\rho}_w^I - \hat{\rho}_f^R d_n - \hat{\rho}_f^I c_n)$ and $g_n^I = 2\pi t_n(\hat{\rho}_w^R + \hat{\rho}_f^I c_n - \hat{\rho}_f^R d_n)$ are the matrix elements.

REFERENCES

- Oppelt A. FISP. A new fast MRI sequence. *Electromedica* 1986;3:15–18.
- Sekihara K. Steady-state magnetizations in rapid NMR imaging using small flip angles and short repetition intervals. *IEEE Trans Med Imaging* 1987;6:157–164.
- Haacke E, Wielopolski P, Tkach J, Modic M. Steady-state free precession imaging in the presence of motion: application for improved visualization of the cerebrospinal fluid. *Radiology* 1990;175:545–552.
- Dixon W. Simple proton spectroscopic imaging. *Radiology* 1984;153:189–194.
- Glover G. Multipoint Dixon technique for water and fat proton and susceptibility imaging. *J Magn Reson Imaging* 1991;1:521–530.
- Vasanawala SS, Pauly JM, Nishimura DG. Fluctuating equilibrium MRI. *Magn Reson Med* 1999;42:876–883.
- Vasanawala SS, Pauly JM, Nishimura DG. Linear combination steady-state free precession MRI. *Magn Reson Med* 2000;43:82–90.
- Scheffler K, Heid O, Hennig J. Magnetization preparation during the steady state: fat-saturated 3D TrueFISP. *Magn Reson Med* 2001;45:1075–1080.
- Hardy PA, Hinks RS, Tkach JA. Separation of fat and water in fast spin-echo MR imaging with the three-point Dixon technique. *J Magn Reson Imaging* 1995;5:181–185.
- Farzaneh F, Riederer SJ, Pelc NJ. Analysis of T2 limitations and off-resonance effects on spatial resolution and artifacts in echo-planar imaging. *Magn Reson Med* 1990;14:123–139.
- Ma J, Singh S, Kumar A, Leeds N, Broemeling L. Phased array coil compatible T2-weighted fast spin echo Dixon imaging. In: *Proceedings of the 10th Annual Meeting of ISMRM, Honolulu, 2002*. p 735.
- Rybicki FJ, Mulkern RV, Robertson RL, Robson CD, Chung T, Ma J. Fast three-point Dixon MR imaging of the retrobulbar space with low-resolution images for phase correction: comparison with fast spin-echo inversion recovery imaging. *AJNR Am J Neuroradiol* 2001;22:1798–1802.
- Roemer P, Edelstein W, Hayes C, Souza S, Mueller O. The NMR phased array. *Magn Reson Med* 1990;16:192–225.
- Hayes C, Roemer P. Noise correlations in data simultaneously acquired from multiple surface coil arrays. *Magn Reson Med* 1990;16:181–191.
- Bernstein M, Grgic M, Brosnan T, Pelc N. Reconstructions of phase contrast, phased array multicoil data. *Magn Reson Med* 1994;32:330–334.
- Kay S. *Fundamentals of statistical signal processing: estimation theory*. Upper Saddle River, NJ: Prentice Hall; 1993. p 83–86.
- Schneider E, Chan TW. Selective MR imaging of silicone with the three-point Dixon technique. *Radiology* 1993;187:89–93.
- Disler DG. Fat-suppressed three-dimensional spoiled gradient-recalled MR imaging: assessment of articular and physal hyaline cartilage. *AJR Am J Roentgenol* 1997;169:1117–1123.
- McCauley TR, Disler DG. MR imaging of articular cartilage. *Radiology* 1998;209:629–640.
- Rybicki FJ, Chung T, Reid J, Jaramillo D, Mulkern RV, Ma J. Fast three-point Dixon MR imaging using low-resolution images for phase correction: a comparison with chemical shift selective fat suppression for pediatric musculoskeletal imaging. *AJR Am J Roentgenol* 2001;177:1019–1023.
- Reeder SB, Pelc NJ, Alley MT, Gold GE. Rapid MR imaging of articular cartilage with steady-state free precession and multipoint fat-water separation. *AJR Am J Roentgenol* 2003;180:357–362.
- Ma J, Singh SK, Kumar AJ, Leeds NE, Broemeling LD. Method for efficient fast spin echo Dixon imaging. *Magn Reson Med* 2002;48:1021–1027.
- Noll DC, Nishimura DG, Macovski A. Homodyne detection in magnetic resonance imaging. *IEEE Trans Med Imaging* 1991;10:154–163.
- Reeder SB, Faranesh AZ, Boxerman JL, McVeigh ER. In vivo measurement of T*2 and field inhomogeneity maps in the human heart at 1.5 T. *Magn Reson Med* 1998;39:988–998.
- Herzka DA, Kellman P, Aletras AH, Guttman MA, McVeigh ER. Multishot EPI-SSFP in the heart. *Magn Reson Med* 2002;47:655–664.
- Oshio K, Feinberg DA. GRASE (gradient- and spin-echo) imaging: a novel fast MRI technique. *Magn Reson Med* 1991;20:344–349.
- Bruder H, Fischer H, Reinfelder HE, Schmitt F. Image reconstruction for echo planar imaging with nonequidistant k-space sampling. *Magn Reson Med* 1992;23:311–323.
- Kwok WE, Totterman SM, Zhong J. 3D interleaved water and fat image acquisition with chemical-shift correction. *Magn Reson Med* 2000;44:322–330.
- Chapra S, Canale R. *Numerical methods for engineers*. 4th ed. Boston: McGraw-Hill; 2002.